Defect-assisted reversible phase transition in mono- and few-layer ReS₂

npj | 2D materials and applications

Article

Published in partnership with FCT NOVA with the support of E-MRS

https://doi.org/10.1038/s41699-025-00524-w

Defect-assisted reversible phase transition in mono- and few-layer ReS_2

George Zograf[1,4], Andrew B. Yankovich[1,4], Betül Küçüköz[1], Abhay V. Agrawal[1], Alexander Yu. Polyakov[1], Joachim Ciers[2], Fredrik Eriksson[1], Åsa Haglund[2], Paul Erhart[1], Tomasz J. Antosiewicz[1,3], Eva Olsson[1] & Timur O. Shegai[1]

2D transition metal dichalcogenide (TMD) materials have attracted interest due to their remarkable excitonic, optical, electrical, and mechanical properties, which are dependent on their crystal structure. Consequently, controlling the crystal structure of these materials is essential for fine-tuning their performance, e.g., linear and nonlinear optical, as well as charge transport properties. While various phase-switching TMD materials are available, their transitions are often irreversible. Here, we investigate the mechanism of a light-induced reversible phase transition in mono- and bilayer rhenium disulfide (ReS_2). Our observations, based on transmission electron microscopy, nonlinear spectroscopy, and density functional theory, reveal a transition from the ground T″ (double-distorted T) to the metastable H′ (distorted H) phase under femtosecond laser irradiation or influence of highly-energetic electrons. We show that the formation of sulfur vacancies facilitates this phenomenon. Our findings pave the way toward manipulating the crystal structure of ReS_2 and possibly its heterostructures.

Over the past two decades, following the seminal work on graphene[1], there has been a substantial growth of interest in atomically thin 2D materials. Among these, transition metal dichalcogenides (TMDs) have emerged as a particularly intriguing family due to their remarkable performance in various nanophotonic[2,3], nanoelectronic[4], and other nanotechnology applications[5]. One highly appealing aspect of TMDs is their versatile nature, which allows for their tuning during device fabrication *via* various control parameters.

TMDs form a diverse material platform comprising transition metal (e.g., Mo, W, Re, Nb, Ta, etc.) and chalcogenide elements (e.g., S, Se, Te). The flexibility to choose these constituent elements during synthesis enables the tunability of TMDs' optical[6] and electronic properties[7]. Furthermore, stacking atomically thin 2D materials in van der Waals heterostructures[8] offers unprecedented control over their properties and can lead to unconventional quantum phenomena, such as superconductivity in graphene-based structures[9,10], Moiré excitons and correlated states in TMDs[11–16], topological excitons[17], advanced excitonic devices[18], and exciton polaritons[19–21]. Following the fabrication of large TMD flakes, achieved through methods like exfoliation[22] or epitaxial single crystal growth[23,24], further modifications of material properties can be realized through nanopatterning, e.g., *via* electron beam lithography (EBL) and chemical etching. Nanopatterning TMDs has enabled the production of high-quality factor (high-Q) nanophotonic structures[25–28], exploration of higher order modes and anapole states[29–32], and lasing from indirect bandgap semiconductor WS_2 microdisks[33]. Expanding control over TMD properties beyond conventional fabrication methods will enable more precise engineering of TMD device performance and deeper insights into the fundamental physics of TMD-related phenomena[34,35].

The ability to actively and reversibly tune TMD properties post-fabrication is of high interest within the 2D material community[36]. Realizing this control to its full potential could expand the range of applications for TMDs, including neuromorphic computing[37,38] as well as optically rewritable electronic circuits and memories[39]. One approach for achieving active control over TMD electronic properties involves photo-induced modifications of the concentration of substitutional and interstitial point defects[40]. Another approach leverages the substantial changes in properties associated with material polymorphism or phase transitions. For instance, entire TMD flakes can undergo phase transitions driven by electrostatic doping[41] or mechanical strain[42]. While these approaches show promise, they typically lack temporal stability and/or precise spatial control at the nanometer scale. Laser-induced phase patterning offers more precise spatial control but is often irreversible due to ablation[43,44], similar to thermal heating during annealing in 2D materials[45]. Nevertheless, promising routes for photo-induced phase switching exist[46,47], such as the reversible transition of TaS_2 into a hidden stable quantum state, enabling drastic changes in conductivity[48,49]. Therefore, exploring new mechanisms for phase

[1]Department of Physics, Chalmers University of Technology, Göteborg, Sweden. [2]Department of Microtechnology and Nanoscience, Chalmers University of Technology, Göteborg, Sweden. [3]Faculty of Physics, University of Warsaw, Warsaw, Poland. [4]These authors contributed equally: George Zograf, Andrew B. Yankovich. e-mail: timurs@chalmers.se

transitions in TMDs and understanding their associated property changes are crucial for achieving improved active control.

Rhenium disulfide (ReS_2) is a promising TMD material for optical, electronic, and gas-sensing applications[50–55]. Its unique features include being a direct bandgap semiconductor in a bulk van der Waals crystal[56] and its high optical anisotropy, making it ideal for directionally selective photonic applications[6,57–60]. Previous investigations have focused on ReS_2's atomic structure and phases using density functional theory (DFT)[56] and scanning transmission electron microscopy (STEM)[61]. Additionally, second-harmonic generation (SHG) studies have linked its activity to stacking and thickness variations[62]. Notably, ReS_2 monolayers (ML) and bilayers (BL) have been demonstrated to exhibit a reversible phase transition under near-infrared femtosecond (fs) laser irradiation, characterized by a significant change in SHG activity and polarization-resolved SHG[63]. It was hypothesized from the available data that ReS_2 transitions from the 1T′ phase into the 1H phase[63]. Despite this promising initial work, questions remain regarding the involved transition phases and the mechanism enabling the transition.

Here, we investigate the phase transition in ReS_2 using a combination of electronic structure calculations, optical SHG microscopy, STEM imaging and diffraction, and electronic transport measurements. Our study results in several key observations: (i) femtosecond laser irradiation induces a phase transition in ReS_2 which converts back to the initial phase with time, (ii) the initial and the "switched" phases are identified as T″ and H′, respectively, with the latter being metastable (as opposed to its unstable H counterpart), and (iii) defects, particularly sulfur vacancies, play a crucial role in facilitating the 1T″-1H′ transition. Our investigation provides a deeper understanding of the possible phases of ML and BL ReS_2 and reveals the importance of vacancy defect formation for the mechanisms of phase switching.

Results and discussion

System under study

The main premise of our work is depicted in Fig. 1. Under intense fs-laser illumination or influence of high-energy electrons, 1T″ ML and 2T″ BL flakes undergo a phase transition into what we hypothesize to be the 1H′ phase, a detailed description of which is provided in the Electronic band structure calculation section below. This phase transition is facilitated by the generation of a sufficient amount of sulfur vacancies that allow the transition to occur by providing the necessary geometrical freedom. The H′ phase is metastable and is protected by an activation energy barrier (E_a), illustrated schematically in Fig. 1a. Successful realization of this phase transition is visually evident in a significantly amplified SHG signal that strongly depends on the crystalline symmetry of the atomic structure, as shown in Fig. 1b for ML ReS_2 using DFT calculations. The atomic rearrangement during the phase transition from 1T″ to 1H′ is illustrated in Fig. 1c.

Our experimental investigation starts with the fabrication of ML and BL ReS_2 flakes on two different substrates *via* mechanical exfoliation and dry transfer from a host crystal. Using this approach, we deposited flakes onto: (i) a silicon/silicon dioxide (Si/SiO_2) substrate for optical and field-effect transistor (FET) transport studies, and (ii) a silicon nitride (SiN) membrane for STEM and electron diffraction studies. More details about the fabrication process are provided in the "Methods" section.

The thickness of the fabricated flakes was identified in three steps: optical imaging, SHG intensity, and atomic-force microscopy (AFM). Optical contrast in reflection microscopy provides an accurate estimation of the thickness of the flake[64,65]. Owing to different symmetries upon stacking, the ReS_2 flakes demonstrate SHG activity depending on the number of layers[62]. Finally, AFM reveals the exact thickness of the most promising flakes (see Supplementary Information (SI), Supplementary Fig. 10).

Evidencing the phase transition in mono- and bilayer ReS_2 by electron microscopy

To directly characterize the unperturbed starting phase of ML and BL ReS_2, as well as the evolution of their atomic structure during defect generation, we conducted experimental and simulated atomic resolution annular dark-field scanning transmission electron microscopy (ADF STEM) and position averaged convergent beam electron diffraction (PACBED) investigations. ADF STEM imaging enables one to directly visualize the positions of the Re

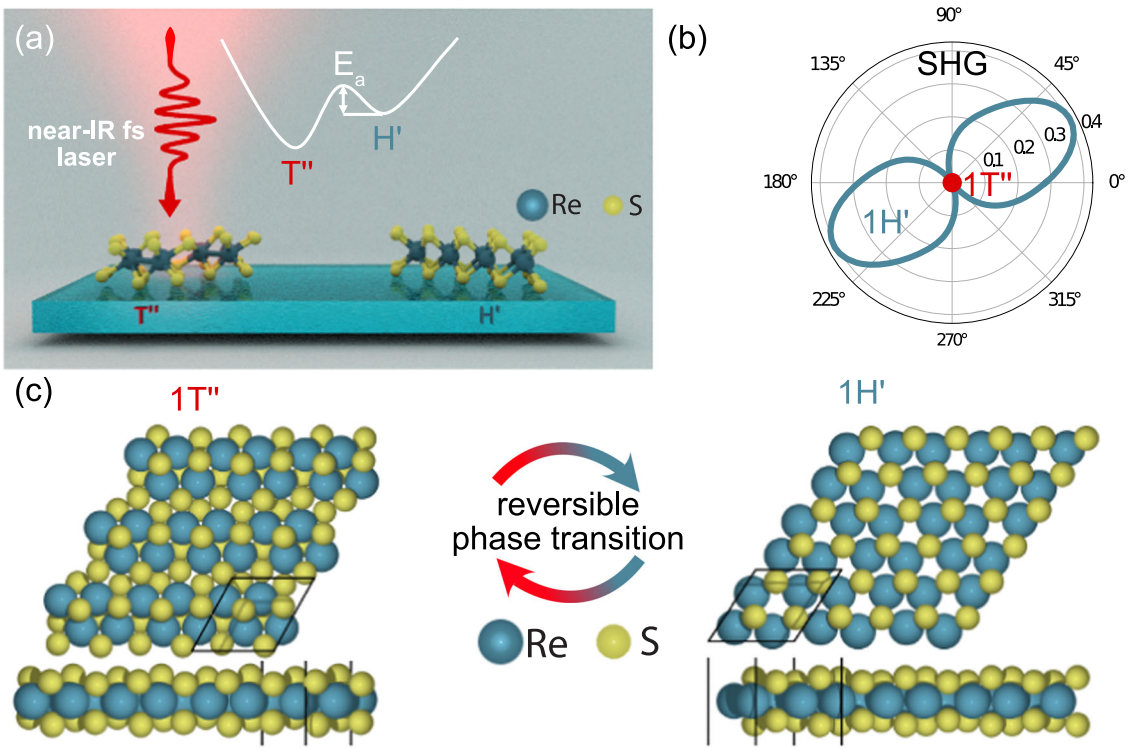

Fig. 1 | Overview. a Schematic of the physical process underpinning the laser-induced phase transition. Femtosecond laser pulses in the near-IR range induce a phase transition from the T″ ground state of ReS_2 flakes into the H′ transient state manifested by a structural change. **b** SHG polarization-resolved intensity of 1T″ and 1H′ monolayer flakes calculated using DFT. **c** Structural changes in the lattice symmetry upon the phase transition between 1T″ and 1H′ monolayer flakes of ReS_2.

atoms (see "Methods" section for more details about the selection of STEM imaging modes and resulting image contrast) and, therefore, the atomic structure evolution. PACBED patterns provide a wealth of structural information about crystalline samples[66,67], such as the phase, by recording momentum-resolved measurements of the forward scattered electrons. PACBED enables the collection of this information from extremely small areas of the sample (down to a single unit cell or even atom[68]), which can be controlled by selecting the sample area where the STEM probe is scanned. PACBED is particularly important to this work because it is sensitive to the electron scattering from both the Re and S atoms, and thus provides a S-sensitive phase characterization tool, in contrast to ADF STEM imaging. To enable these investigations, exfoliated ML and BL flakes were transferred to ~20 nm thick SiN membrane TEM grids (see "Methods" section for further details).

We identify the structure of unperturbed ML ReS_2 using ADF STEM imaging and PACBED while considering 5 possible ML ReS_2 phases: 1H, 1T, 1T′, 1T″, and 1H′. The experimental atomic resolution ADF STEM image of unperturbed ML ReS_2 in Fig. 2a and the associated template-averaged image in Fig. 2a,i reveals the positions of the Re atoms and the presence of a double-distorted structure that is indicated by the red diamonds. A simulated ADF STEM image of the 1T″ phase is shown in the lower right inset image in Fig. 2a,ii. The similarity between the experimental (Fig. 2a,i) and simulated (Fig. 2a,ii) ADF STEM images, as well as the dissimilarity between the experimental ADF STEM image and simulated images of the other possible ML ReS_2 phases (see Supplementary Fig. 3), provide evidence that unperturbed ML ReS_2 has the 1T″ phase. In addition, the experimental PACBED pattern from ML ReS_2 (Fig. 2b,i) is in best agreement with the simulated PACBED pattern from the 1T″ phase (Fig. 2b,ii and Supplementary Fig. 3) providing further evidence that unperturbed ML ReS_2 has the 1T″ phase. Our findings are in agreement with previous studies[69], further supporting that monolayer ReS_2 adopts the 1T″ configuration.

Electron beam irradiation is known to introduce damage to TMD materials, primarily through a knock-on sputtering process that introduces chalcogenide vacancies[70]. For the unperturbed phase measurements, special experimental design and analysis were conducted to ensure there were negligible effects from the electron beam irradiation on the phase identification (see "Methods" section for more details). However, we also leveraged the chalcogenide vacancies production mechanism to design ADF STEM imaging experiments that resolve the atomic structure evolution of ML and BL ReS_2 during increasing S-vacancy concentrations. This is achieved by acquiring time-resolved ADF STEM image series with carefully selected electron beam energy, electron dose, and STEM image scan parameters (see "Methods" section).

During time-resolved ADF STEM imaging experiments on ML ReS_2 (see Supplementary Movies 1 and 2 for example image series), electron irradiation damage occurs very rapidly, partially because experiments are limited to using a 200 keV electron beam due to sample constraints (see "Methods" section for more details). Similar behavior was observed in ML $MoTe_2$ during lower voltage TEM experiments[71]. The image series shown in Supplementary Movies 1 and 2 reveal that ML ReS_2 undergoes a complete destruction of its 2D crystallinity after a few tens of image frames (see "Methods" section for dose values). After a complete loss of the 2D crystalline structure, it appears as though Re nanoclusters remain, providing evidence that the damage occurs through a sulfur sputtering and vacancy generation mechanism. Interestingly, just prior to the loss of the 2D crystallinity, ML ReS_2 undergoes a rearrangement of its atomic structure from a double-distorted 1T″ phase to what appears like nano-sized regions of a *single distorted* nonstoichiometric phase that can have three possible in-plane orientations. Figure 2c,i–iv shows extracted images from areas adjacent to and after Supplementary Movie 2. Figure 2c,i shows the starting 1T″ phase, while Fig. 2c,ii–iv show the three possible orientations of the resulting single distorted structure that are rotated by 60° from each other. Supplementary Fig. 2 provides details on the image locations of Fig. 2c,i–iv and a Fast Fourier transform analysis of these nano-sized regions that confirms a clear change in structure and a 60° rotation between possible single distorted phase regions. Because the ADF STEM images are only sensitive to the Re atoms and not the S atoms, we can not unambiguously identify the resulting single distorted phase using this measurement. However, this investigation reveals ML ReS_2 transitions from the 1T″ phase to a single distorted nonstoichiometric phase that is consistent with 1H′ (Supplementary Fig. 3). Furthermore, the 1H′ phase is consistent with our SHG data and DFT calculations, as we show below.

We now use ADF STEM imaging and PACBED to identify the structure of unperturbed BL ReS_2. For this analysis, we consider 15 possible BL ReS_2 phases, including 2H, 2T, 2T′, and twelve different 2T′ phases (named 2T″c-n) that have previously been explored as possible stable phases[72]. The experimental atomic resolution ADF STEM image of unperturbed BL ReS_2 in Fig. 2d and the associated template-averaged image in Fig. 2d,i reveals the presence of a stacked double-distorted structure that is indicated by the red and blue diamonds. A simulated ADF STEM image of the 2T″e phase is shown in Fig. 2d,ii. The similarity between the experimental, Fig. 2d,i, and simulated, Fig. 2d,ii ADF STEM images, as well as the dissimilarity between the experimental ADF STEM image and simulated images of the other possible BL ReS_2 phases (see Supplementary Figs. 7 and 8), provides evidence that unperturbed BL ReS_2 has the 2T″e phase. In addition, the experimental PACBED pattern from BL ReS_2, Fig. 2e,i, is in best agreement with the simulated PACBED pattern from the 2T″e phase (Fig. 2e,ii, Supplementary Fig. 6, Supplementary Fig. 9) providing further evidence that unperturbed BL ReS_2 has the 2T″e phase. After considering all 12 possible phases, we can conclude unperturbed BL ReS_2 has the 2T″ phase and most likely the 2T″e variant.

Time-resolved ADF STEM imaging experiments also provide evidence for electron beam-induced phase transitions in BL ReS_2. Supplementary Movies 7 and 8 (see "Methods" section for data processing details and Supplementary Movies 5-6 for unprocessed versions) are two consecutive image series of the same area that show BL ReS_2 exhibits obvious structural changes during electron beam irradiation before eventually losing its 2D crystallinity. This is similar to what was observed for ML ReS_2, except BL ReS_2 requires a substantially higher electron dose for a complete loss of 2D crystallinity (see "Methods" section for dose values). Additionally, it undergoes what appears like three distinct atomic structure transitions before it loses its 2D crystallinity. Fig. 2f,i–iv are extracted images from Supplementary Movies 7 and 8 at four different times (see "Methods" section). Fig. 2f,i shows the initial 2T″e phase characterized by the two stacked red and blue diamonds. After electron irradiation and the generation of S-vacancies, the structure transitions through 3 distinct phases shown in Fig. 2f,ii–iv. Fig. 2f,ii and iii show the atomic structure transitions through what appears like two different single distorted phases. Following this, the final phase is characterized by the loss of the double and single distortion axes of the Re atoms and the presence of a hexagonal structure (see green hexagon in Fig. 2f,iv). Based on the atomic column contrast in Fig. 2f,iv, each column appears to contain two Re atoms stacked in an A-A stacking configuration. Because the S atoms are invisible in these ADF STEM images and they are critical to identifying an H or T phase, it is not possible to unambiguously identify the transitional phases from this data (the T phase is, however, inconsistent with our SHG data, discussed below). Despite this, we can conclude the electron irradiation and the subsequent generation of S-vacancies causes BL ReS_2 to evolve from a starting double-distorted 2T″ phase into nano-sized domains of two different non-stoichiometric single distorted phases before losing its Re distortion axes completely and transitioning into an A-A stacked hexagonal nonstoichiometric structure with a subsequent loss of its 2D crystallinity, leaving behind Re nanoclusters. Although we can not extract the S-vacancy concentration throughout this evolution, we expect the S-vacancy concentration to continuously increase during this process with the total electron dose, highlighting the critical role of defects in enabling the T″–H′ transition.

Light-induced phase transition

We now turn our attention to light-induced phase transition in ReS_2. In these experiments, we use a Si/SiO_2 substrate with a 285-nm-thick SiO_2 layer. We start our analysis by studying the time-dependent formation of the

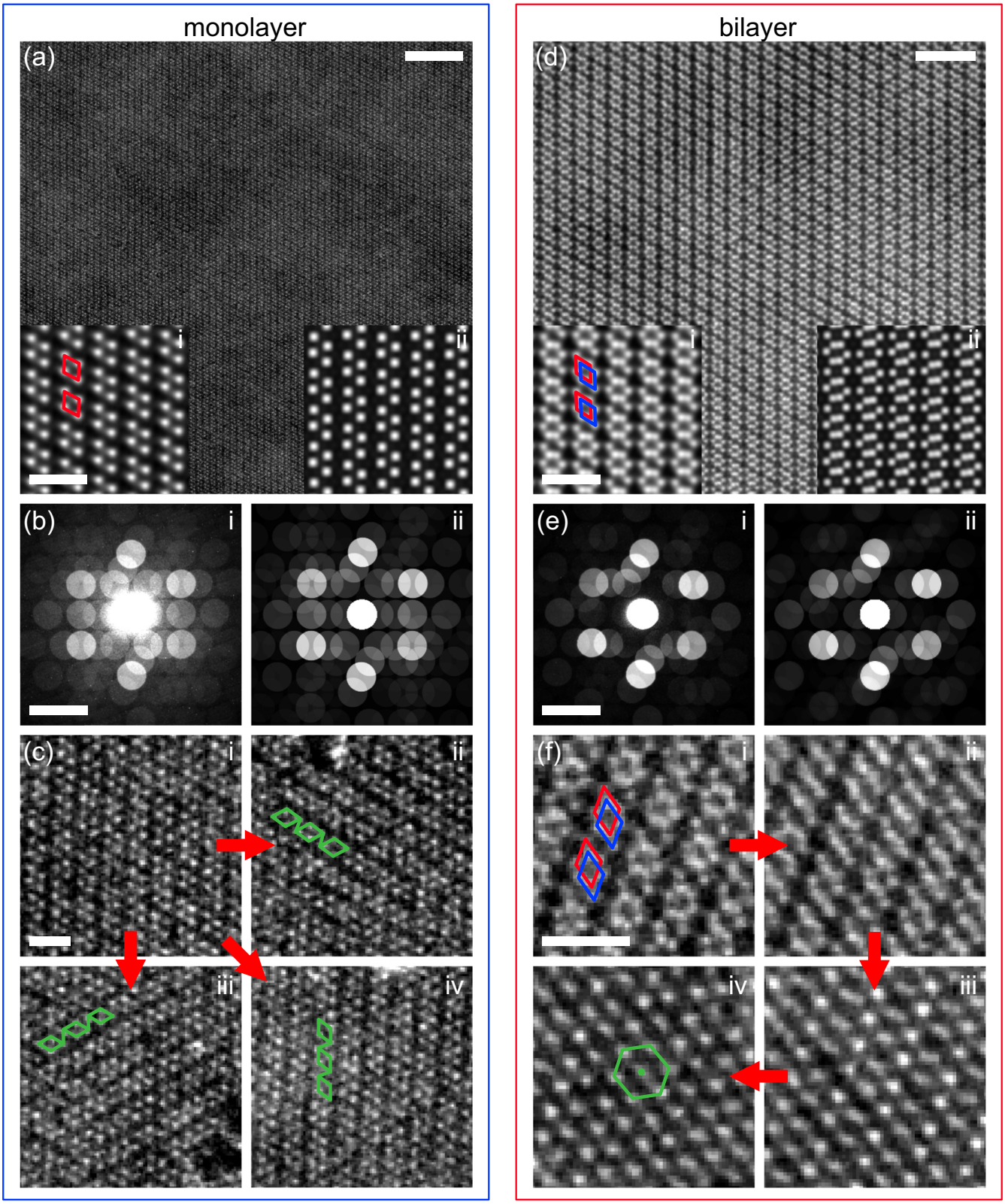

SHG-active 1H′ phase. In this experiment, the fs-laser beam was focused on a specific location on the ML ReS_2 flake, with a new spot selected for each excitation power. The SHG intensity was continuously monitored as a function of time during the exposure. Fig. 3a depicts the time evolution of the SHG intensity signal from different areas of the ReS_2 ML flake. The colors of the curves from blue to red demonstrate the increase of the incident 1040 nm wavelength fs-laser power. One can see similar features in every curve for different powers: (i) some time delay, or, as we introduce, the lag time τ_{lag} before the SHG intensity begins to substantially increase (the rate is the time in the power of three), (ii) flattening or saturation of the signal after reaching a certain level of counts. The analysis of the lag time τ_{lag} or the inverted lag time τ_{lag}^{-1} as a function of incident power will give us information

Fig. 2 | ML and BL ReS_2 STEM observations. a Experimental ADF STEM image of undamaged ML ReS_2. The scale bar is 5 nm. The lower left inset image is a template-matched average image produced from the entire image in (**a**). The lower right inset image is a simulated ADF STEM image of the 1T″ phase. The scale bar is 1 nm in both inset images. **b**(i) Experimental PACBED pattern of undamaged ML ReS_2. **b**(ii) Simulated PACBED pattern of the 1T″ phase. The scale bar is 0.6 inverse Angstroms in both **b**(i) and **b**(ii). **c** Experimental ADF STEM images from different regions of electron-irradiated ML ReS_2. The scale bar is 1 nm. **c**(i) is from an undamaged 1T″ region. **c**(ii–iv) are from different damaged regions that exhibit a loss of the 1T″ phase but maintain a dominant distorted axis that rotates by 60° around the out-of-plane c-axis to produce three possible in-plane orientations. The green markers represent the rearrangement of Re atoms upon phase transition. **d** Experimental ADF STEM image of undamaged BL ReS_2. The lower left inset image is a template-matched average image produced from the entire image in (**d**). The lower right inset image is a simulated ADF STEM image of the 2T″e phase. The scale bar is 1 nm in both inset images. **e**(i) Experimental PACBED pattern of undamaged BL ReS_2. **e**(ii) Simulated PACBED pattern of the 2T″e phase. The scale bar is 0.6 inverse Angstroms in both **e**(i) and **e**(ii). **f** Experimental ADF STEM images extracted from an image series showing the atomic structure evolution of BL ReS_2 due to electron beam irradiation. The scale bar is 1 nm. **f**(i) shows the initial undamaged structure that is consistent with the 2T″e phase. **f**(ii–iv) shows three distinct structures that are observed in sequence during electron beam irradiation, which are followed by complete destruction of the 2D crystalline lattice. The green markers represent the rearrangement of Re atoms upon phase transition.

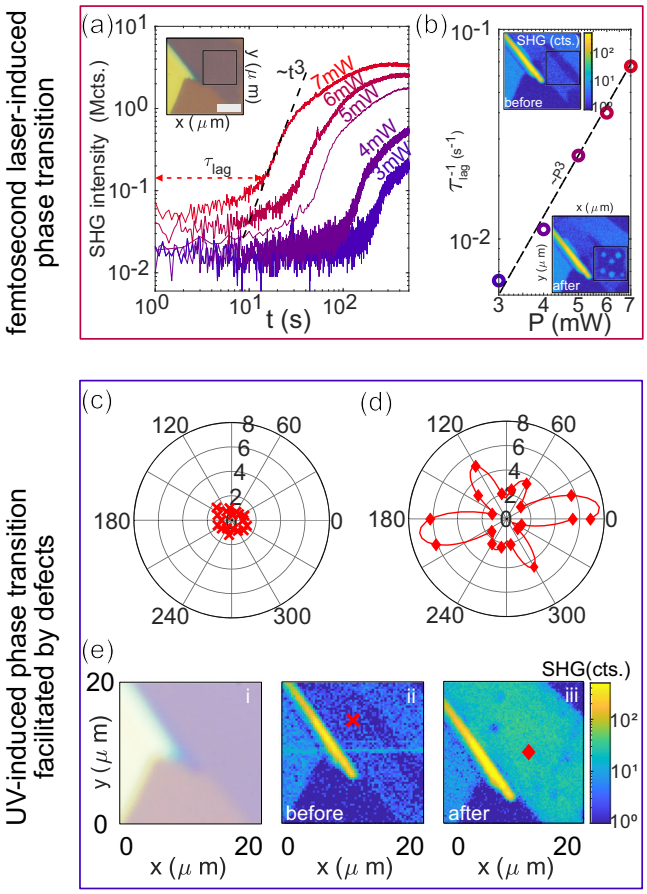

Fig. 3 | Defect-induced phase transition in ReS_2 flakes. a Time evolution of SHG counts for ReS_2 monolayer at 1040 nm fs-laser-induced point (static position of the laser beam) patterning process at different incident powers. τ_{lag} is the specific time of the SHG counts dramatic increase. The dashed line corresponds to the third-power slope. The inset depicts the optical image of the flake, with the black square indicating the area of interest. The scale bar is 5 μm. **b** The rate of the phase transition (inverted τ_{lag}) as a function of incident power of the fs-laser at 1040 nm pump wavelength. The color of the experimental points corresponds to the same color as in the time evolution curve in (**a**). The dashed line corresponds to the third-power slope. Insets depict the SHG map before (upper) and after (lower) laser point patterning. **c** and **d** are polarization-resolved SHG polar plots obtained from respective areas of (**e**) - red cross (**e**.ii - pristine) and red diamond (**e**.iii - exposed to moderate UV light). The flake after the formation of fs-laser-induced defects studied in (**a**, **b**) is subsequently exposed to UV light (**e**.iii). **e** also shows an optical image of the flake (**e**.i).

on how soon the phase transition begins. Fig. 3b depicts exactly this with a clear third-order dependence of the incident power, meaning doubling the power will result in an 8-fold quicker initiation of the phase transition of the ReS_2 ML on a 285 nm Si/SiO_2 substrate. This finding is of interest for patterning extended ReS_2 areas, as shown in comparison in the insets of Fig. 3b before exposure (upper) and after exposure (lower), since it allows us to precisely determine the necessary and sufficient conditions for the phase transition to occur. The reason behind such two-phase behavior and the dependence of the lag time on fs-laser power might arise from two key processes – multiple photon absorption of the flake for transition into the 1H′ phase and the phase transition nucleation and growth process, which requires defect formation. As we discuss in detail below, the latter is in line with the increase in the SHG intensity signal of the patterned ReS_2 bilayer with the number of cycles of fs-laser patterning that the particular sample underwent, as shown in Fig. 5a – crosses. Additionally, it has been reported that ReS_2 MLs tend to host point defects more likely than, for example, MoS_2 as the covalent bond is rather soft in the 1T″ double-distorted phase[73,74]. Further evidence for defect formation comes from the FET data (see Supplementary Fig. 13). Notably, the current in the patterned structures drops by nearly two orders of magnitude, indicating defect formation. This observation is in line with previous studies that report degradation in transport properties due to the formation of sulfur vacancies in e.g. MoS_2[75].

Once the ML is heavily patterned by fs-laser (bottom inset Fig. 3b) and, therefore, hosts enough defects, one can induce a phase transition from 1T″ into 1H′ phase using an ultraviolet (UV) source at significantly smaller power compared to the fs-laser (see "Methods" section). Notably, without such pre-patterning by the fs-laser, UV light alone can not trigger the phase transition (see Supplementary Fig. 12), suggesting that it is insufficient to generate defects. This also suggests that switching and defect formation processes can be effectively decoupled, allowing UV-induced switching to occur without the need for further defect generation. In addition, we stress that the UV experiment was performed across the entire flake using an unfocused light, affecting both areas directly exposed to the fs-laser pre-patterning and those farther away. Both regions successfully transitioned to the new phase, supporting the nucleation and growth hypothesis underlying this phase transition. The polarization-resolved SHG plots in Fig. 3c, d before and after patterning manifest significant changes in the structure upon UV exposure. The pronounced 3 pairs of 2-fold symmetric SHG profiles with 60° shifts between each other in the patterned case indicate the formation of a different phase. The three 2-fold symmetries are in line with the STEM observations in Fig. 2c and data provided in SI, which indicate that upon phase transition ML ReS_2 forms distinct domains with the *b*-axes in each domain oriented 60° with respect to each other. Individually, each domain yields an SHG spectrum with 2-fold symmetry, as calculated in Fig. 1b, but there is no guarantee that in a given SHG measurement the surface area of the three mutually rotated 1H′ domains will be equal. Hence, in general, the SHG signal is expected to be characterized by three 2-fold symmetric profiles. Moreover, the intensity of the SHG from the ML in Fig. 3e confirms the phase transition. The AFM data (see Supplementary Fig. 10) of the studied ReS_2 flake confirms its monolayer nature.

We validate the defect-assisted nature of the light-induced phase transition in ReS_2 through various experimental techniques, including fs-laser patterning, SHG polarization-resolved spectroscopy, UV-induced phase switching, and photoluminescence (PL) (the latter is discussed in SI, Supplementary Fig. 11). Furthermore, using the Si/SiO_2 substrate allows for conducting both optical and FET experiments and therefore gaining a deeper understanding of the electronic conductivity properties (see

Supplementary Fig. 13). We note that the final phase of the ReS_2 can not be unambiguously identified solely from the SHG data, however, we conclude that ReS_2 switches into either H or H′ due to SHG intensity and polarization-resolved data pointing to the broken inversion symmetry of the lattice. Together with ADF STEM presented earlier and the subsequent discussion on DFT, we propose the hypothesis of T″–H′ phase transitions, as this scenario aligns consistently with all the experimental and theoretical methods used in our study as well as with observations from previously published work[63]. Specifically, our observations indicate that a certain level of defects is necessary to facilitate the T″–H′ phase transition. These defects are induced either by fs-laser irradiation or exposure to energetic electrons, presenting an excited state pathway for the T″–H′ transition. The 1H′ phase is metastable due to the presence of an activation energy barrier, and once defects are introduced, the transition from the 1T″ phase to the 1H′ phase can be initiated by various external stimuli, such as UV light, fs-laser pulses, or fast electrons. The formation of defects is irreversible, as evidenced by the irreversibility of the PL and FET measurements, which do not revert to their initial performance (see SI for details). However, the phase change in terms of SHG activity can be almost completely reversed at elevated temperatures, as discussed below.

Electronic structure calculations

Our STEM and SHG data indicate a phase transition to a state with broken inversion symmetry. A reasonable first assumption is that the transition involves the standard undistorted H phase, similar to that of monolayers MoS_2, WS_2, and others[63]. However, electronic structure calculations reveal that this phase is unstable in monolayer ReS_2[52,69], see Fig. 4. This suggests that another phase, exhibiting broken inversion symmetry, likely underlies the observed SHG and STEM behaviors. STEM data further reveal that the "switched" phase is distorted (see Fig. 2c), confirming its distinction from the 1H phase. Hence, we propose that this phase corresponds to 1H′ (the distorted 1H phase; space group Amm2, see Fig. 1c). Our numerical simulations, incorporating phononic and electronic band structure diagrams (see Fig. 4), indicate the stability of the 1H′ phase and its potential accessibility from 1T″ *via* high-energy excitations utilizing photons (both multi- and single-photon processes are possible) or electrons (see Fig. S2). These calculations confirm that the 1H phase is unstable and therefore unlikely to be responsible for the observed behavior. Instead, ReS_2 tends to switch into a metastable 1H′ semimetal state, which aligns with our experimental observations in ADF STEM and SHG. To our knowledge, this is the first demonstration of the existence and stability of the 1H′ phase in ReS_2.

Our calculations suggest the involvement of sulfur vacancies in facilitating the T″–H′ phase transition. Furthermore, they also suggest the reduced energy required to form sulfur vacancies in the 1H′ phase compared to 1T″. The role of the sulfur defects consists in providing the necessary space for the transition to occur. Importantly, both the direct T″ to H′ and reverse H′ to T″ phase transitions require synchronized motion of large numbers of sulfur atoms, which can only occur when there is sufficient geometrical freedom to perform such motion. Additionally, molecular dynamics simulations demonstrate that the back-transition from 1H′ to 1T″ requires S-vacancies and represents a first-order phase transition involving nucleation and growth of one (switched) phase within the continuum of another (unswitched) phase (data not shown), confirming the role of sulfur vacancies. These predictions align with both light- and electron-induced 1T″–1H′ phase transitions observed in SHG, STEM, and FET measurements, as all of them require and indicate defect formation prior to the transition (for instance, see UV-induced phase change data, Fig. 3c–e, and Supplementary Figs. 12 and 13). Finally, it is important to note that the reverse transition from 1H′ to 1T″ can not be induced by light due to the significant differences in their electronic band structures and corresponding absorption spectra (see Fig. 4).

The SHG pattern of the proposed 1H′ phase can be simulated by using the $\chi^{(2)}$ tensor obtained from density functional theory (DFT) and yields a polarization-dependent profile with two distinct lobes (Fig. 1b). Our

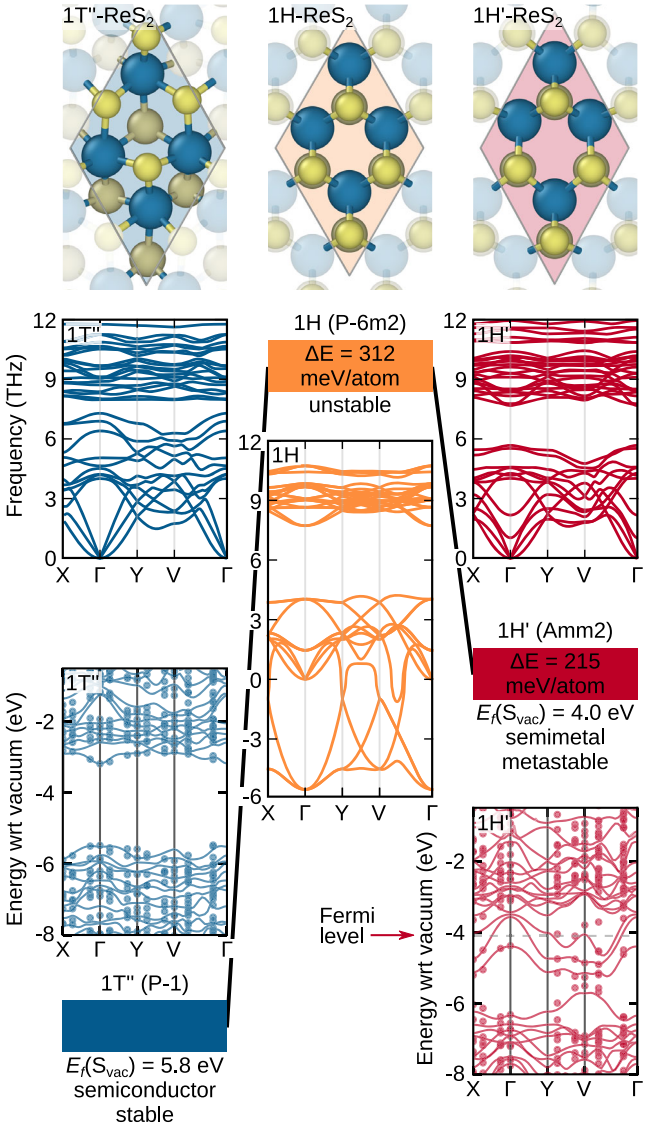

Fig. 4 | DFT analysis of monolayer ReS_2 phases. Left: stable 1T″ semiconducting phase. Middle: unstable 1H phase. Right: metastable 1H′ semimetal phase.

experimental SHG data suggest the existence of three possible orientation domains within the 1H′ phase (rotated with respect to each other by 60°). Their stochastic combination accounts for a 6-fold-like symmetric pattern (Fig. 3d), where SHG lobes vary in length, reflecting the prevalence of specific orientations in the final orientation domain composite (see STEM data in Fig. 2c).

Although numerical electronic structure calculations offer substantial support for the existence and relative stability of the 1H′ phase, alongside information about sulfur vacancies and second-order optical nonlinearities, they lack precision in estimating the activation energy barrier for the reverse H′ to T″ transition, which is crucial to characterize the stability of the H′ phase. Thus, in the subsequent section, we shift our focus to experimental observations of this back-switching process. The metastability of the H′ phase implies its eventual inevitable return to the stable T″ phase, with the switching rate following a temperature-dependent Arrhenius-like behavior, as we demonstrate below.

Estimation of the activation energy barrier in bilayer ReS_2

We use a pristine BL flake of ReS_2 to study the activation energy barrier height for the reverse transition from the H′ to the T″ phase. Unlike an ML (see Fig. 3), the BL is highly SHG-active[62,63], which is reflected in the

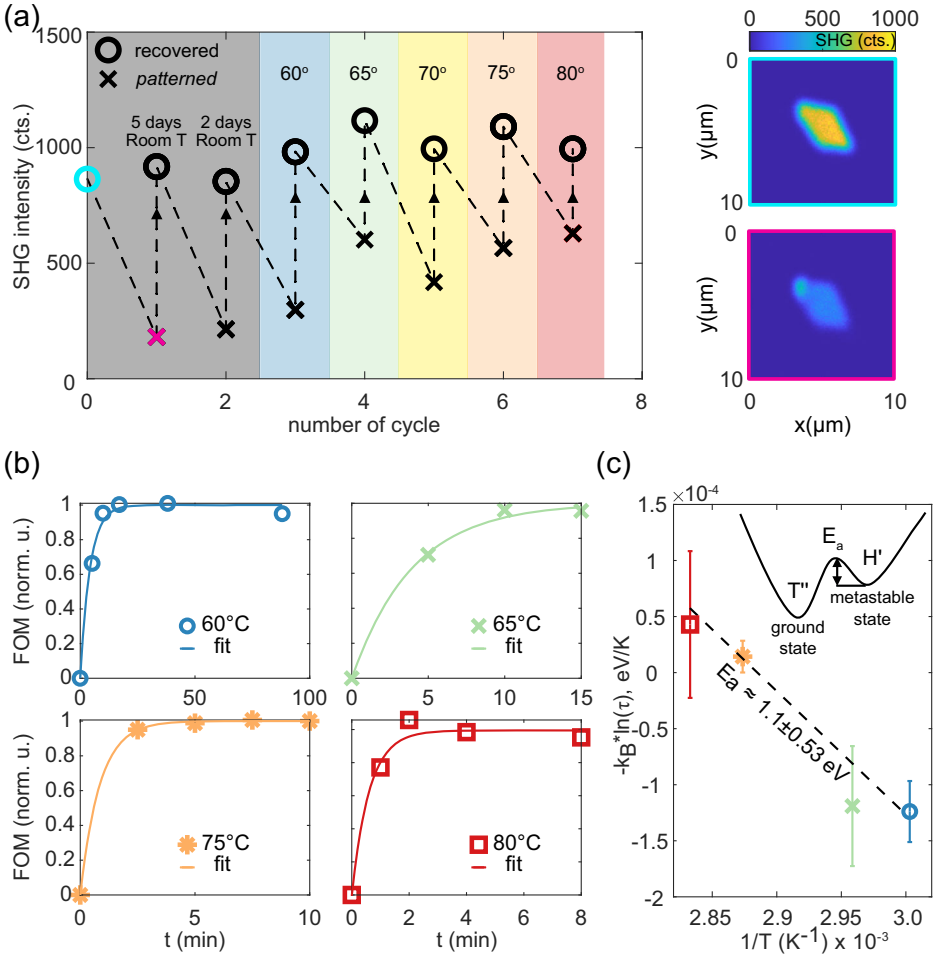

Fig. 5 | Fs-laser-induced patterning mechanism. **a** The average SHG intensity over the flake upon several patterning-recovery cycles of a bilayer ReS_2 flake. Circles correspond to the counts of SHG-active 2T″ of a bilayer, while crosses correspond to SHG counts of a 2H′ phase. The right side panels (highlighted in cyan and magenta) demonstrate the SHG maps of a bilayer before and after the 1st patterning, respectively. All the patterning cycles were carried out at the same conditions of the fs-laser – 8 mW average power, 400 ms exposure, and a 50 nm spatial step. The recovery conditions are specified above each recovered point. The colored regions correspond to the conditions of the recovery of the same color in (**b**) and (**c**). **b** Recovery FOM(t,T) as a function of time for different temperature values that stimulates the recovery process. The lines indicate a single exponential fit for the recovery process. **c** Arrhenius plot showing logarithm of recovery rate ($1/\tau$) *vs.* inverted temperature at which the recovery process was measured. The linear fitting reflects the energy activation barrier, $E_a = 1.10 \pm 0.53$ eV, between the phases. Colors and symbols correspond to the same colors and symbols as in (**b**). Inset is the sketch of the energy diagram corresponding to the thermally-induced H′ – T″ recovery process.

upper inset with a cyan frame of Fig. 5a. Upon fs-laser patterning of the area with specific step size (50 nm), exposure time (400 ms), and power (8 mW), the flake significantly reduces the counts of the SHG signal, indicating the phase transition from the T″ into H′ phase (see Fig. 5a, lower inset with a magenta frame). After some time, the sample recovers its initial SHG intensity counts, signaling the reverse transition to the pristine state. By applying the exposure conditions multiple times after each recovery, we repeated the patterning process 7 times for the bilayer to prove the reversibility of the phase transition, as shown in Fig. 5a. The circles depict the recovered (or pristine for the first cyan circle) SHG-active T″ bilayer states, whereas the crosses mark the patterned SHG-inactive H′ ones. Notably, we observe a clear trend that the difference in SHG signal between the circles and crosses is reducing with the number of cycles. This may be attributed to incomplete phase switching caused by irreversible degradation or permanent damage of the material triggered by multiple exposures to the fs-laser.

Another important parameter is the time the BL ReS_2 flake resides in the metastable H′ phase. Importantly, the recovery time is strongly temperature-dependent (see Fig. 5a). At room temperature, the sample takes several days to return to its initial state, whereas at elevated temperatures, the relaxation process occurs within minutes. By measuring the duration of this recovery process at different temperatures, we aim to conduct an Arrhenius-like analysis to estimate the activation energy barrier (E_a) between the ground T″ phase and the metastable H′ phase. With that in mind, we introduce the phase transition recovery figure-of-merit (FOM), which relies on the SHG intensity as a measure of the phase transition. If the I_{rec} is the SHG intensity of the recovered bilayer flake, then $\mathrm{FOM}(t,T) = \frac{I_T(t)}{I_{rec}}$, where T is the temperature of the flake, t is the time after the patterning took place, and $I_T(t)$ – the intensity of the SHG of the flake at a particular moment t and at specific temperature T. For a range of temperatures from 60 °C to 80 °C with a 5 °C step size, we performed a series of the measurements of the FOM(t,T) as shown in Fig. 5b, for the same sample from Fig. 5a. FOM = 0 right at the moment of a freshly patterned flake (2H′), whereas FOM = 1 means that the sample recovered to its initial SHG intensity (2T″). The sample recovery curves at different temperatures can be fitted with a single exponential growth function – $\mathrm{FOM}(t,T) = 1 - e^{-t/\tau}$, with a characteristic time scale, τ. The rate of the reverse phase transition is, therefore, τ^{-1}. The normalized SHG intensities as a function of recovery time (symbols), along with the corresponding fits (solid lines), are shown in Fig. 5b for various temperatures. Then, for every particular temperature, we plot the logarithm of τ^{-1} multiplied by the value of the Boltzmann constant. Furthermore, we fit the $-\ln(\tau)$ versus $1/T$ using a linear function and obtain $E_a = 1.10 \pm 0.53$ eV with 95% confidence (see Fig. 5c). The experimental point corresponding to 70 °C was excluded from this analysis due to an insufficient number of measurements, resulting in large errors in this case. The fitting procedure includes the error bars of the extracted values of τ for every temperature condition. Based on these experimental findings, we deduce that the stabilization energy barrier for the 2H′ phase is of the order of 1 eV. The phase transition diagram is schematically depicted in Fig. 5c. Initially, the H′ phase can not form due to the insufficient number of defects. However, upon fs-laser-induced multiphoton absorption, combined with the simultaneous creation of S-vacancies, a new excited state relaxation pathway opens up, enabling the formation of the metastable H′ phase through the first-order phase transition, which involves nucleation and growth.

In this study, we present evidence of a reversible phase transition occurring in mono-, bi-, and trilayer ReS_2. The transition occurs from the T″ to the H′ phase at room temperature and ambient conditions. Through a combination of several experimental and theoretical methods, including

electron microscopy, second-order nonlinear spectroscopy, photoluminescence, electronic transport, and DFT calculations, we identify that the transition is consistent with the formation of the metastable H′ (distorted H) phase. Notably, our data suggest a crucial role of sulfur vacancies in enabling this transition. Our analysis also confirms the ground state phase of the ReS_2 ML and BL flakes to be 1T″ and 2T″, respectively. Furthermore, we experimentally determine the activation energy barrier for the reverse H′ to T″ transition in BL ReS_2 to be approximately 1.10 ± 0.53 eV. From a broader perspective, these results expand the knowledge of light- and electron-induced phase-switching materials and offer insights into the potential for optically programmable properties of TMD-based devices.

Methods

Sample fabrication

The ReS_2 flakes were mechanically exfoliated from the high-quality bulk crystal (HQ Graphene) using scotch tape with a subsequent transfer on polydimethylsiloxane stamps (PDMS) in a cleanroom (Nanofabrication laboratory at Chalmers within MyFab). For the STEM experiments, ReS_2 flakes were transferred to 20 nm thick SiN membrane TEM grids (simpore.com) using an all-dry transfer method[76]. For the laser patterning and all the optical measurements, the flakes were transferred from the PDMS stamps to the glass slides. For the electrical transport measurements, ReS_2 flakes were transferred to the 285-nm thick Si/SiO_2 highly *n*-doped substrates (Graphene Supermarket, USA) with pre-fabricated 20 nm Cr/200 nm Au back contact. To produce source and drain top contacts for ReS_2 flakes, a ~300 nm layer of 950 PMMA A4 resist (MicroChem, USA) was applied by spin-coating. PMMA was patterned by e-beam lithography employing a Raith EBPG 5200 (Germany) system operating at 100 kV accelerating voltage and 30 nA current. A dose of 1300 μC/cm^2 was applied, and 1:3 MIBK:IPA mixture was used as a developer. Then, the 5 nm Cr/200 nm Au layer was evaporated by Lesker PVD 225 e-beam evaporation system (Kurt J. Lesker Company, Germany). Overnight lift-off in acetone was used to finalize the contact fabrication.

Optical measurements

Second-harmonic generation (SHG) measurements were carried out using (690–1040 nm) Ti:sapphire femtosecond laser (MaiTai HP-Newport Spectra-Physics) with a ~100 fs pulse duration and 80 MHz repetition rate as an excitation source. The light was polarized linearly with a broadband linear polarizer and focused through an objective (Nikon, 40×, NA = 0.95). The positioning of the sample was controlled both in the plane ($x - y$) and the focus (z) by the piezoelectric motorized stage. The signal was collected with an avalanche photo-diode for mapping (APD, IDQ, ID100 Visible Single-Photon Detector) or spectrometer (Andor 500*i*, equipped with Newton 920 CCD camera) through an optical fiber. The polarization-resolved SHG measurements were performed on the same setup using $\lambda/2$ plate to rotate the linear polarization of the excitation light. For SHG imaging, we utilized a tightly focused 1040 nm laser beam with 2 mW power, employing a 250 nm scanning step and a 5 ms exposure time per spot. Under these imaging conditions, the ReS_2 phase transition was not triggered.

Photoluminescence (PL) measurements were carried out on the inverted optical microscopy setup using a high-NA oil immersion objective (Nikon, 60×, NA = 1.49). The excitation 447 nm continuous-wave laser was coupled to an optical fiber and focused on the bottom side of the sample through the objective. A 488 nm long-pass filter is placed in the detection path to remove the laser excitation from the PL signal. The setup allows for rotating the incident linear polarization and offers the possibility for an analyzer in the signal collection channel.

Light-induced phase transition conditions

In the case of fs-laser-induced transitions, defect formation, and the light-induced phase transition occur at the same time. For patterning the ReS_2 flake, we utilized a tightly focused (close to diffraction limit) 1040 nm laser beam with 8 mW power (average intensity of ~10^6 W/cm^2, peak intensity of ~1.25×10^{11} W/cm^2), 80 MHz repetition rate, and a 100 fs pulse duration. The sample patterning conditions were consistent across all fs-laser experiments, employing a 50 nm scanning step and a 400 ms exposure time per spot. These conditions resulted in significantly higher laser exposure compared to the SHG-imaging conditions specified above and were sufficient to induce the phase transition.

For phase transition using UV illumination, ReS_2 flakes were exposed to an *unfocused* quasi-CW 237 nm nanosecond laser with an average intensity of 0.01 W/cm^2 (peak intensity of 1182 W/cm^2) for one hour.

STEM measurements and calculations

STEM imaging and PACBED experiments were carried out on a JEOL Mono NEO ARM 200F microscope. ADF STEM imaging was conducted using an accelerating voltage of 200 kV, a probe convergence half-angle of 26.7 mrad, an ADF detector collection angle range of 65–146 mrad, and a probe current of 44 picoampere (pA). In order to improve the quality of the ADF STEM images for the atomic structure analyses, a combination of non-rigid registration of image series[77] and template matching was used depending on the specific data set. PACBED experiments[66] were conducted using an accelerating voltage of 80 kV, a probe convergence half-angle of 6.35 mrad, and a probe current of <3 pA. To resolve the ML and BL ReS PACBED patterns more clearly, careful corrections of the detector dark signal and SiN support signal were manually performed. ADF STEM and PACBED simulations were calculated using the frozen phonon multislice algorithm implemented in the GPU-accelerated software Prismatic 2.0[78].

The ADF STEM collection angle range of 65–146 mrad produces Z-contrast images[79–81] where primarily the Re atom positions are visible while the S positions are invisible. Other collection angles more suitable for light-element imaging, such as annular bright field STEM imaging[82], yielded poor results due to the signal from the SiN support.

The accelerating voltage of 200 kV was selected because lower voltages made it more difficult to achieve sufficient atomic contrast of the Re atoms above the SiN support background intensity. The accelerating voltage of 200 kV is above the known knock-on threshold energy for sulfur vacancy generation in TMD materials[70]. However, the 44 picoamperes (pA) probe current and 4–32 μs/pixel dwell times were sufficient to image ReS_2 before significant structural damage occurred. These beam conditions enabled the observation of both the initial undamaged atomic structure and the dynamic evolution of the atomic structure as sulfur vacancies were generated.

For PACBED experiments, an accelerating voltage of 80 kV was beneficial for two primary reasons. First, it minimized damage to the sample and enabled long PACBED exposure times, which were required to reveal the weak ML and BL diffraction signals above the noise level. 80 kV is slightly above the knock-on damage threshold for most TMD materials[70], but subsequent PACBED acquisitions of the same area showed no signs of a changing structure and damage. Second, lowering the accelerating voltage increases the Bragg scattering angles of the ReS_2 diffraction signals. This effectively separates the diffraction disks, causes less disc overlap, and makes it easier to identify PACBED patterns from different phases. PACBED patterns were acquired by scanning the STEM beam over a 10–20 nm^2 area for 300 s while continuously acquiring the diffraction pattern. This acquisition technique enables sufficient sampling and position-averaging of probe positions over the structure to produce high-quality PACBED patterns, and it distributes the electron dose over a larger area to minimize sample damage. To see the ML and BL ReS_2 PACBED patterns more clearly, careful corrections of the dark signal and SiN support signal were manually performed. The dark signal was corrected by subtracting a reference dark pattern that was acquired directly after the ReS_2 PACBED pattern. The SiN support adds a diffuse amorphous signal to the PACBED pattern. This SiN support signal was removed by subtracting a reference pattern that was acquired from only the SiN support near the flake. The dark and SiN reference patterns were acquired with the same acquisition parameters as the ReS_2 patterns. The resulting PACBED patterns were binned by 4×4 pixels to enhance the signal-to-noise ratio and gain more clarity in the diffraction signals.

The ADF STEM image shown in Fig. 2a is a single-pass STEM image acquired with a size of 1024 × 1024 pixels, a dwell time of 32 µs/pixel, a pixel size of 0.039 nm/pixel, a flyback time of 500 µs, and a total electron dose of 6×10^4 e Å^{-2}. All of the doses reported in this publication include the dose associated with the line flyback time. The template-matched average image shown in the lower left inset image of Fig. 2a is the average of 3195 template images from within Fig. 2a. The template images that were selected for the averaging were determined using an in-house written IGOR Pro script that locates the maxima in the normalized cross-correlation between a user-selected input template image and all other possible template images (see Supplementary Fig. 1 for more details).

The ADF STEM images shown in Fig. 2c are sub-regions extracted from a single-pass STEM image that was acquired directly after a higher magnification image series which damaged the ML. The single-pass image is shown in Supplementary Fig. 2 and was acquired with a size of 1024 × 1024 pixels, a dwell time of 64 µs/pixel, a pixel size of 0.048 nm/pixel, a flyback time of 500 µs, and a total electron dose of 7.6×10^4 e Å^{-2}. Supplementary Fig. 2 also shows the locations of the cropped images displayed in Fig. 2c and their associated FFTs, which further show the changes in atomic structure and orientation. The higher magnification image series that damaged the ML is shown in Supplementary Movie 2 and was acquired at the center of the single-pass image shown in Supplementary Fig. 2. The image series was acquired with 100 frames, a size of 512 × 512 pixels, a dwell time of 16 µs/pixel, a pixel size of 0.02 nm/pixel, a flyback time of 500 µs, and a total electron dose of 1.2×10^7 e Å^{-2}. An additional ADF STEM image series that reveals the dynamics of the structural changes caused by electron irradiation is shown in Supplementary Movie 1. It was acquired with 100 frames, a size of 1024 × 1024 pixels, a dwell time of 4 µs/pixel, a pixel size of 0.016 nm/pixel, a flyback time of 500 µs, and a total electron dose of 4.8×10^6 e Å^{-2}. The series displayed in Supplementary Movie 1 was spatially binned by 4 × 4 pixels and smoothed with a 3 × 3 pixels Gaussian to improve the signal-to-noise ratio and enhance the visibility of the atomic structure.

The ADF STEM image shown in Fig. 2d is an average of an image time series that was non-rigidly registered[77] to correct the effects of the microscope, sample, and environmental instabilities. The image series was acquired with 50 frames, a size of 512 × 512 pixels, a dwell time of 8 µs/pixel, a pixel size of 0.04 nm/pixel, a flyback time of 500 µs, and a total electron dose of 7.9×10^5 e Å^{-2}. The non-rigidly registered and a temporally binned version are shown in Supplementary Movies 3 and 4, respectively. These movies, in combination with Supplementary Fig. 4, show that negligible structural damage was caused by the electron irradiation. The template-matched average image shown in the lower left inset image of Fig. 2d is the average of 843 template images from within Fig. 2d that were determined using the same process discussed above for Fig. 2a (see Supplementary Fig. 5 for more details).

The ADF STEM images shown in Fig. 2f are sub-regions extracted from frames of an image time series that damaged the bilayer. The total image series is composed of two separate consecutively acquired image series of the same sample area, each of which was acquired with 50 frames, a size of 512 × 512 pixels, a dwell time of 16 µs/pixel, a pixel size of 0.0395 nm/pixel, a flyback time of 500 µs, and a total electron dose of 1.5×10^6 e Å^{-2}. Each image series was non-rigidly registered[77] to correct the effects of the microscope, sample, and environmental instabilities. Both series were temporally binned by 5 frames to improve the signal-to-noise ratio and the visibility of the structural changes, producing an image series with 10 frames. The images shown in Fig. 2f (main text) are extracted regions from (i) frame 1 of 10 in series 1, (ii) frame 10 of 10 in series 1, (iii) frame 4 of 10 in series 2, and (iv) frame 10 of 10 in series 2. These 4 images have been smoothed with a 3 × 3 pixel Gaussian to improve the signal-to-noise ratio and enhance the visibility of the atomic structure. The non-rigidly registered image series are provided in Supplementary Movies 5 and 6 and the temporally binned image series are provided in Supplementary Movies 7 and 8.

ADF STEM and PACBED simulations were calculated using the frozen phonon multislice algorithm implemented in the GPU-accelerated software Prismatic 2.0[78]. DFT relaxed atomic models of the different ML and BL phases were used as input structures for the calculations. All calculations utilized root-mean-square displacements of 0.045 Å and 0.077 Å for the Re and S atoms, respectively. ML ADF STEM image simulations were performed with an accelerating voltage of 200 keV, a STEM probe convergence half-angle of 26.69 mrad, 10 phonon configurations, atomic models with a size of around 150 Å × 150 Å, a potential space sampling of 0.04 Å, an ADF detector range of 50–155 mrad, and a probe step size of 0.1 Å. ML PACBED simulations were performed with an accelerating voltage of 80 kV, a STEM probe convergence half-angle of 6.35 mrad, 10 phonon configurations, atomic models with a size of around 150 Å × 150 Å, a potential space sampling of 0.05 Å, and a probe step size of around 1.6 Å, which is sufficient for Nyquist sampling. Bilayer ADF STEM image simulations were performed with an accelerating voltage of 200 kV, a STEM probe convergence half-angle of 26.69 mrad, 10 phonon configurations, atomic models with a size of around 50 Å × 50 Å, a potential space sampling of 0.03 Å, an ADF detector range of 50–155 mrad, and a probe step size of 0.05 Å. Bilayer PACBED simulations were performed with an accelerating voltage of 80 kV, a STEM probe convergence half-angle of 6.35 mrad, 30 phonon configurations, atomic models with a size of around 100 Å × 100 Å, a potential space sampling of 0.1 Å, and a probe step size of around 1.6 Å, which is sufficient for Nyquist sampling.

Electrical transport measurements

FET measurements were conducted using two source channel -measurement units (B2901A, Keysight) connected through a General Purpose Interface Bus (GPIB) cable with a computer. The typical FET measurements were performed at room temperature. The back-gate voltage was systematically adjusted within the range of −10 V to 10 V, while simultaneously tuning the source-drain voltage between −1 V and 1 V.

Electronic structure calculations

The energetics of different phases, their dynamic stability, defect formation energies, and electronic band structures were obtained *via* DFT calculations that were carried out using the projector augmented-wave method[83] as implemented in the Vienna ab initio simulation package[84,85]. The exchange-correlation potential was represented using the van der Waals density functional with consistent exchange method[86,87]. All calculations were carried out using a plane-wave energy cutoff of 520 eV and for the calculation of the forces, a finer support grid was employed to improve their numerical accuracy. The Brillouin zone was sampled using Γ-centered grid with a linear $\vec{k}$-point spacing of about 0.25 Å^{-1} and Gaussian smearing with a width of 0.1 eV. This setup has been previously employed and tested for other layered materials[88,89].

For the ideal 1A and Amm2 structures the electronic band structures were furthermore computed using the G_0W_0 method[90] on a Γ-centered $8 \times 8 \times 1$ grid. These calculations employed 282 empty bands, thereby including states up to at least 28 eV above the valence band edge (1 A) or Fermi level (Amm2), and used 50 imaginary frequency and time grid points.

Phonon dispersions were computed *via* the PHONOPY package[91] in combination with the HIPHIVE package[92] using force constants from DFT calculations.

The $\chi^{(2)}$ polarizability tensor was calculated using the method and tools outlined by Taghizadeh et al.[93]. Briefly, we calculated the nonlinear optical response using the DFT open-source GPAW package[94,95]. We used the PBE exchange-correlation functional[96], the Kohn–Sham orbitals were expanded using a plane-wave basis set with an energy cutoff of 500 eV, we used a $21 \times 21 \times 3$ Monkhorst–Pack grid for the k-mesh and a grid spacing of less than 0.2 Å. The number of empty bands included in the sum over bands was set to three times the number of occupied bands. We used Fermi–Dirac occupation number smearing with a factor of 20 meV and line-shape broadening of 50 meV. Time-reversal symmetry was imposed in order to reduce the k-integrals to half.

Data availability

Data generated during the study is available upon reasonable request from the corresponding author.

Received: 21 May 2024; Accepted: 29 December 2024;
Published online: 14 January 2025

References

1. Novoselov, K. S. et al. Electric field effect in atomically thin carbon films. *Science* **306**, 666–669 (2004).
2. Mak, K. F. & Shan, J. Photonics and optoelectronics of 2D semiconductor transition metal dichalcogenides. *Nat. Photon.* **10**, 216–226 (2016).
3. Trovatello, C. et al. Optical parametric amplification by monolayer transition metal dichalcogenides. *Nat. Photon.* **15**, 6–10 (2021).
4. Radisavljevic, B., Radenovic, A., Brivio, J., Giacometti, V. & Kis, A. Single-layer MoS_2 transistors. *Nat. Nanotechnol.* **6**, 147–150 (2011).
5. Manzeli, S., Ovchinnikov, D., Pasquier, D., Yazyev, O. V. & Kis, A. 2D transition metal dichalcogenides. *Nat. Rev. Mater.* **2**, 1–15 (2017).
6. Munkhbat, B., Wróbel, P., Antosiewicz, T. J. & Shegai, T. O. Optical constants of several multilayer transition metal dichalcogenides measured by spectroscopic ellipsometry in the 300–1700 nm range: High index, anisotropy, and hyperbolicity. *ACS Photonics* **9**, 2398–2407 (2022).
7. Wang, Q. H., Kalantar-Zadeh, K., Kis, A., Coleman, J. N. & Strano, M. S. Electronics and optoelectronics of two-dimensional transition metal dichalcogenides. *Nat. Nanotechnol.* **7**, 699–712 (2012).
8. Geim, A. K. & Grigorieva, I. V. Van der Waals heterostructures. *Nature* **499**, 419–425 (2013).
9. Balents, L., Dean, C. R., Efetov, D. K. & Young, A. F. Superconductivity and strong correlations in moiré flat bands. *Nat. Phys.* **16**, 725–733 (2020).
10. Cao, Y. et al. Unconventional superconductivity in magic-angle graphene superlattices. *Nature* **556**, 43–50 (2018).
11. Fang, Y. et al. Discovery of superconductivity in 2M WS_2 with possible topological surface states. *Adv. Mater.* **31**, 1901942 (2019).
12. Jin, C. et al. Observation of moiré excitons in WSe_2/WS_2 heterostructure superlattices. *Nature* **567**, 76–80 (2019).
13. Alexeev, E. M. et al. Resonantly hybridized excitons in moiré superlattices in van der Waals heterostructures. *Nature* **567**, 81–86 (2019).
14. Brem, S., Linderälv, C., Erhart, P. & Malic, E. Tunable phases of Moiré excitons in van der Waals heterostructures. *Nano Lett.* **20**, 8534 (2020).
15. Tang, Y. et al. Simulation of Hubbard model physics in WSe_2/WS_2 moiré superlattices. *Nature* **579**, 353–358 (2020).
16. Huang, X. et al. Correlated insulating states at fractional fillings of the WS_2/WS_2 moiré lattice. *Nat. Phys.* **17**, 715–719 (2021).
17. Wu, F., Lovorn, T. & MacDonald, A. H. Topological exciton bands in moiré heterojunctions. *Phys. Rev. Lett.* **118**, 147401 (2017).
18. Ciarrocchi, A., Tagarelli, F., Avsar, A. & Kis, A. Excitonic devices with van der Waals heterostructures: valleytronics meets twistronics. *Nat. Rev. Mater.* **7**, 449–464 (2022).
19. Zhang, L. et al. Van der Waals heterostructure polaritons with moiré-induced nonlinearity. *Nature* **591**, 61–65 (2021).
20. Munkhbat, B., Canales, A., Küçüköz, B., Baranov, D. G. & Shegai, T. O. Tunable self-assembled Casimir microcavities and polaritons. *Nature* **597**, 214–219 (2021).
21. Dirnberger, F. et al. Magneto-optics in a van der Waals magnet tuned by self-hybridized polaritons. *Nature* **620**, 533–537 (2023).
22. Huang, Y. et al. Universal mechanical exfoliation of large-area 2D crystals. *Nat. Commun.* **11**, 2453 (2020).
23. Dumcenco, D. et al. Large-area epitaxial monolayer MoS_2. *ACS Nano* **9**, 4611–4620 (2015).
24. Li, T. et al. Epitaxial growth of wafer-scale molybdenum disulfide semiconductor single crystals on sapphire. *Nat. Nanotechnol.* **16**, 1201–1207 (2021).
25. Munkhbat, B. et al. Transition metal dichalcogenide metamaterials with atomic precision. *Nat. Commun.* **11**, 1–8 (2020).
26. Munkhbat, B., Küçüköz, B., Baranov, D. G., Antosiewicz, T. J. & Shegai, T. O. Nanostructured transition metal dichalcogenide multilayers for advanced nanophotonics. *Laser Photonics Rev.* **17**, 2200057 (2023).
27. Weber, T. et al. Intrinsic strong light-matter coupling with self-hybridized bound states in the continuum in van der Waals metasurfaces. *Nat. Mater.* **22**, 970–976 (2023).
28. Zotev, P. G. et al. Van der waals materials for applications in nanophotonics. *Laser Photonics Rev.* **17**, 2200957 (2023).
29. Verre, R. et al. Transition metal dichalcogenide nanodisks as high-index dielectric Mie nanoresonators. *Nat. Nanotechnol.* **14**, 679–683 (2019).
30. Tselikov, G. I. et al. Transition metal dichalcogenide nanospheres for high-refractive-index nanophotonics and biomedical theranostics. *Proc. Natl Acad. Sci. USA* **119**, 2208830119 (2022).
31. Maciel-Escudero, C. et al. Probing optical anapoles with fast electron beams. *Nat. Commun.* **14**, 8478 (2023).
32. Zograf, G. et al. Combining ultrahigh index with exceptional nonlinearity in resonant transition metal dichalcogenide nanodisks. *Nat. Photon.* **18**, 751–757 (2024).
33. Sung, J. et al. Room-temperature continuous-wave indirect-bandgap transition lasing in an ultra-thin WS_2 disk. *Nat. Photon.* **16**, 792–797 (2022).
34. Ling, H., Li, R. & Davoyan, A. R. All van der waals integrated nanophotonics with bulk transition metal dichalcogenides. *ACS Photonics* **8**, 721–730 (2021).
35. Ling, H. et al. Deeply subwavelength integrated excitonic van der Waals nanophotonics. *Optica* **10**, 1345–1352 (2023).
36. Li, W., Qian, X. & Li, J. Phase transitions in 2D materials. *Nat. Rev. Mater.* **6**, 829–846 (2021).
37. Chialvo, D. R. Emergent complex neural dynamics. *Nat. Phys.* **6**, 744–750 (2010).
38. Marković, D., Mizrahi, A., Querlioz, D. & Grollier, J. Physics for neuromorphic computing. *Nat. Rev. Phys.* **2**, 499–510 (2020).
39. Wuttig, M. & Yamada, N. Phase-change materials for rewriteable data storage. *Nat. Mater.* **6**, 824–832 (2007).
40. Seo, S.-Y. et al. Reconfigurable photo-induced doping of two-dimensional van der Waals semiconductors using different photon energies. *Nat. Electron.* **4**, 38–44 (2021).
41. Wang, Y. et al. Structural phase transition in monolayer $MoTe_2$ driven by electrostatic doping. *Nature* **550**, 487–491 (2017).
42. Voiry, D. et al. Enhanced catalytic activity in strained chemically exfoliated WS_2 nanosheets for hydrogen evolution. *Nat. Mater.* **12**, 850–855 (2013).
43. Cho, S. et al. Phase patterning for ohmic homojunction contact in $MoTe_2$. *Science* **349**, 625–628 (2015).
44. Guan, Y. et al. Femtosecond laser-driven phase engineering of WS_2 for nano-periodic phase patterning and sub-ppm ammonia gas sensing. *Small* **19**, 2303654 (2023).
45. Yu, Y. et al. High phase-purity $1T'$-MoS_2- and $1T'$-$MoSe_2$-layered crystals. *Nat. Chem.* **10**, 638–643 (2018).
46. Nasu, K. *Photoinduced Phase Transitions* (World Scientific, Singapore, 2004).
47. Yang, H., Kim, S. W., Chhowalla, M. & Lee, Y. H. Structural and quantum-state phase transitions in van der Waals layered materials. *Nat. Phys.* **13**, 931–937 (2017).
48. Stojchevska, L. et al. Ultrafast switching to a stable hidden quantum state in an electronic crystal. *Science* **344**, 177–180 (2014).
49. Vaskivskyi, I. et al. A high-efficiency programmable modulator for extreme ultraviolet light with nanometre feature size based on an electronic phase transition. *Nat. Photon.* **18**, 458–463 (2024).
50. Zhang, E. et al. ReS_2-based field-effect transistors and photodetectors. *Adv. Funct. Mater.* **25**, 4076–4082 (2015).
51. Pradhan, N. R. et al. Metal to insulator quantum-phase transition in few-layered ReS_2. *Nano Lett.* **15**, 8377–8384 (2015).
52. Rahman, M., Davey, K. & Qiao, S.-Z. Advent of 2D rhenium disulfide (ReS_2): fundamentals to applications. *Adv. Funct. Mater.* **27**, 1606129 (2017).

53. Xiang, D. et al. Anomalous broadband spectrum photodetection in 2D rhenium disulfide transistor. *Adv. Opt. Mater.* **7**, 1901115 (2019).
54. Gogna, R., Zhang, L. & Deng, H. Self-hybridized, polarized polaritons in ReS_2 crystals. *ACS Photonics* **7**, 3328–3332 (2020).
55. Xiong, X. et al. Nonvolatile logic and ternary content-addressable memory based on complementary black phosphorus and rhenium disulfide transistors. *Adv. Mater.* **34**, 2106321 (2022).
56. Tongay, S. et al. Monolayer behaviour in bulk ReS_2 due to electronic and vibrational decoupling. *Nat. Commun.* **5**, 3252 (2014).
57. Lin, Y.-C. et al. Single-layer ReS_2: two-dimensional semiconductor with tunable in-plane anisotropy. *ACS Nano* **9**, 11249–11257 (2015).
58. Chenet, D. A. et al. In-plane anisotropy in mono-and few-layer ReS_2 probed by Raman spectroscopy and scanning transmission electron microscopy. *Nano Lett.* **15**, 5667–5672 (2015).
59. Liu, F. et al. Highly sensitive detection of polarized light using anisotropic 2D ReS_2. *Adv. Funct. Mater.* **26**, 1169–1177 (2016).
60. Ermolaev, G. A. et al. Wandering principal optical axes in van der Waals triclinic materials. *Nat. Commun.* **15**, 1552 (2024).
61. Zhou, Y. et al. Stacking-order-driven optical properties and carrier dynamics in ReS_2. *Adv. Mater.* **32**, 1908311 (2020).
62. Song, Y. et al. Extraordinary second harmonic generation in ReS_2 atomic crystals. *ACS Photonics* **5**, 3485–3491 (2018).
63. Küçüköz, B., Munkhbat, B. & Shegai, T. O. Boosting second-harmonic generation in monolayer rhenium disulfide by reversible laser patterning. *ACS Photonics* **9**, 518–526 (2022).
64. Castellanos-Gomez, A., Agraït, N. & Rubio-Bollinger, G. Optical identification of atomically thin dichalcogenide crystals. *Appl. Phys. Lett* **96**, 213116 (2010).
65. Anzai, Y. et al. Broad range thickness identification of hexagonal boron nitride by colors. *Appl. Phys. Express* **12**, 055007 (2019).
66. LeBeau, J. M., Findlay, S. D., Allen, L. J. & Stemmer, S. Position averaged convergent beam electron diffraction: theory and applications. *Ultramicroscopy* **110**, 118–125 (2010).
67. Ophus, C. Four-dimensional scanning transmission electron microscopy (4D-STEM): from scanning nanodiffraction to ptychography and beyond. *Microsc. Microanal.* **25**, 563–582 (2019).
68. Zhang, C., Feng, J., DaCosta, L. R. & Voyles, P. M. Atomic resolution convergent beam electron diffraction analysis using convolutional neural networks. *Ultramicroscopy* **210**, 112921 (2020).
69. Pasquier, D. & Yazyev, O. V. Unified picture of lattice instabilities in metallic transition metal dichalcogenides. *Phys. Rev. B* **100**, 201103 (2019).
70. Komsa, H.-P. et al. Two-dimensional transition metal dichalcogenides under electron irradiation: defect production and doping. *Phys. Rev. Lett.* **109**, 035503 (2012).
71. Köster, J. et al. Phase transformations in single-layer $MoTe_2$ stimulated by electron irradiation and annealing. *Nanotechnology* **35**, 145301 (2024).
72. Qiao, X.-F. et al. Polytypism and unexpected strong interlayer coupling in two-dimensional layered ReS_2. *Nanoscale* **8**, 8324–8332 (2016).
73. Horzum, S. et al. Formation and stability of point defects in monolayer rhenium disulfide. *Phys. Rev. B* **89**, 155433 (2014).
74. Huang, J. et al. Enhanced photoelectrochemical performance of defect-rich ReS_2 nanosheets in visible-light assisted hydrogen generation. *Nano Energy* **46**, 305–313 (2018).
75. Bertolazzi, S. et al. Engineering chemically active defects in monolayer mos2 transistors via ion-beam irradiation and their healing via vapor deposition of alkanethiols. *Adv. Mater.* **29**, 1606760 (2017).
76. Castellanos-Gomez, A. et al. Deterministic transfer of two-dimensional materials by all-dry viscoelastic stamping. *2D Mater.* **1**, 011002 (2014).
77. Yankovich, A. B. et al. Picometre-precision analysis of scanning transmission electron microscopy images of platinum nanocatalysts. *Nat. Commun.* **5**, 4155 (2014).
78. DaCosta, L. R. et al. Prismatic 2.0–simulation software for scanning and high resolution transmission electron microscopy (STEM and HRTEM). *Micron* **151**, 103141 (2021).
79. Pennycook, S. J. Z-contrast stem for materials science. *Ultramicroscopy* **30**, 58–69 (1989).
80. Nellist, P. D. & Pennycook, S. J. The principles and interpretation of annular dark-field z-contrast imaging. In *Advances in Imaging and Electron Physics*, Vol. 113 147–203 (Elsevier, 2000).
81. Krivanek, O. L. et al. Atom-by-atom structural and chemical analysis by annular dark-field electron microscopy. *Nature* **464**, 571–574 (2010).
82. Findlay, S. et al. Dynamics of annular bright field imaging in scanning transmission electron microscopy. *Ultramicroscopy* **110**, 903–923 (2010).
83. Blöchl, P. E. Projector augmented-wave method. *Phys. Rev. B* **50**, 17953–17979 (1994).
84. Kresse, G. & Hafner, J. Ab initio molecular dynamics for liquid metals. *Phys. Rev. B* **47**, 558–561 (1993).
85. Kresse, G. & Furthmüller, J. Efficiency of ab-initio total energy calculations for metals and semiconductors using a plane-wave basis set. *Comput. Mater. Sci.* **6**, 15–50 (1996).
86. Dion, M., Rydberg, H., Schröder, E., Langreth, D. C. & Lundqvist, B. I. Van der Waals density functional for general geometries. *Phys. Rev. Lett.* **92**, 246401 (2004).
87. Berland, K. & Hyldgaard, P. Exchange functional that tests the robustness of the plasmon description of the van der Waals density functional. *Phys. Rev. B* **89**, 035412 (2014).
88. Lindroth, D. O. & Erhart, P. Thermal transport in van der Waals solids from first-principles calculations. *Phys. Rev. B* **94**, 115205 (2016).
89. Eriksson, F., Fransson, E., Linderälv, C., Fan, Z. & Erhart, P. Tuning the lattice thermal conductivity in van-der-Waals structures through rotational (dis)ordering. *ACS Nano* **17**, 25565 (2023).
90. Hedin, L. & Lundqvist, S. Effects of electron-electron and electron-phonon interactions on the one-electron states of solids. In: Frederick Seitz, D. T., Ehrenreich, H. (eds.) *Solid State Physics*, Vol. 23 1–181 (Elsevier, 1970).
91. Togo, A. & Tanaka, I. First principles phonon calculations in materials science. *Scr. Mater.* **108**, 1–5 (2015).
92. Eriksson, F., Fransson, E. & Erhart, P. The hiphive package for the extraction of high-order force constants by machine learning. *Adv. Theory Simul.* **2**, 1800184 (2019).
93. Taghizadeh, A., Thygesen, K. S. & Pedersen, T. G. Two-dimensional materials with giant optical nonlinearities near the theoretical upper limit. *ACS Nano* **14**, 7155–7167 (2021).
94. Mortensen, J. J., Hansen, L. B. & Jacobsen, K. W. Real-space grid implementation of the projector augmented wave method. *Phys. Rev. B* **71**, 035109 (2005).
95. Enkovaara, J. et al. Electronic structure calculations with GPAW: a real-space implementation of the projector augmented-wave method. *J. Phys.: Condens. Matter* **22**, 253202 (2010).
96. Perdew, J. P., Burke, K. & Ernzerhof, M. Generalized gradient approximation made simple. *Phys. Rev. Lett.* **77**, 3865–3868 (1996).

Acknowledgements

We thank B. Munkhbat (DTU) for the ReS_2 sample that has been studied in TEM. T.O.S. acknowledges funding from the Swedish Research Council (VR, research environment grant No. 2016-06059, VR projects, grant No. 2017-04545 and No. 2022-03347), Chalmers Area of Advance Nano, 2D-TECH VINNOVA competence center (Ref. 2019-00068) and Olle Engkvist foundation (grant No. 211-0063). A.B.Y., E.O., P.E., and T.O.S. acknowledge funding from the Knut and Alice Wallenberg Foundation (KAW, grant No. 2019.0140). A.B.Y. acknowledges funding from the Swedish Research Council (VR, grant No. 2020-04986). T.J.A. acknowledges funding from the Polish National Science Center, project 2019/34/E/ST3/00359. This work was performed in part at Myfab Chalmers and the Chalmers Material Analysis Laboratory (CMAL). The DFT computations were enabled by resources provided by the Swedish

National Infrastructure for Computing (SNIC) at NSC, C3SE, and PDC partially funded by the Swedish Research Council through grant agreement No. 2018-05973 and by the ICM-UW (Grant #G55-6).

Author contributions

G.Z., A.B.Y., B.K., E.O., and T.O.S. conceived the project idea. G.Z. and B.K. performed optical measurements. A.B.Y. performed and analyzed STEM and PACBED data. A.V.A. performed FET measurements. A.Y.P. fabricated the samples for FET experiments. J.C. and Å.H. assisted with UV experiments. F.E., P.E., and T.J.A. calculated dispersion with DFT. T.J.A. calculated the nonlinear response of the flakes. G.Z., A.B.Y, and T.O.S. wrote the manuscript with contributions from all co-authors.

Funding

Open access funding provided by Chalmers University of Technology.

Competing interests

The authors declare no competing interests.

Additional information

Supplementary information The online version contains supplementary material available at https://doi.org/10.1038/s41699-025-00524-w.

Correspondence and requests for materials should be addressed to Timur O. Shegai.